www.czasopisma.pan.pl PAN POLSKA AKADEMIA NAUK www.journals.pan.pl

Archives of Acoustics Vol. **48**, No. 4, pp. 509–521 (2023), doi: 10.24425/aoa.2023.146821

Research Paper

Impulse Excitation in a Watertight Steel Circular Cylindrical Shell and Influence of Structural Configuration on Underwater Radiated Noise

Chen-I WU*, Gee-Pinn TOO, Bo-Hsien WU

Department of Systems and Naval Mechatronic Engineering, National Cheng Kung University
Tainan, Taiwan

*Corresponding Author e-mail: kpssi3006@gmail.com

(*received September 4, 2022; accepted June 20, 2023*)

This study used experimental measurements and the finite-element method (FEM) simulations to investigate transient underwater radiated noise induced by the impulse excitation of water surrounding a watertight steel-structured circular cylindrical shell submerged in the $176 \times 8 \times 4$ m towing tank. The excitation was caused by dropping an iron block onto a structural bracket in the shell to generate structural vibration. The experimental results were found to be consistent with the FEM results, with the difference between the experimental and simulated sound pressure levels being less than 3 dB. Moreover, it was determined that the structural vibration also generated airborne noise in the cylindrical shell, but this contributed much less than the impulse excitation to the induction of underwater radiated noise. Finally, analysis of the sound field of the underwater noise radiation showed that it was influenced by the wall thickness of the watertight steel cylindrical shell and that of the reinforced bracket seat structure. In particular, the structural reinforcement position proved to be the diffusion breakpoint of the underwater sound radiation. This demonstrates that compared with the studied structure, a thicker and more complex reinforced structure will transmit less or incomplete sound radiation into water.

Keywords: impulse excitation; influence of structural configuration; FEM analysis; underwater noise radiation characteristics.

1. Introduction

Understanding the characteristics of noise radiated from underwater vehicles is a key research challenge. As underwater noise radiation is influenced by the structure of underwater vehicles, vehicle-induced underwater noise can be predicted by model simulation, and underwater noise and structure-borne noise caused by vibrating structures can be determined by testing experimental models. In this study, hydrophones were used to measure the underwater noise-radiation sound field caused by an impulse-induced vibration in a model underwater vehicle. In addition, the underwater noise-radiation sound field was numerically simulated using the finite-element method (FEM).

The underwater radiated noise was generated by dropping an iron block onto a section of a model underwater vehicle inside a watertight steel circular cylindrical shell submerged in water in the $176 \times 8 \times 4$ m towing tank. The experimental setup was remotely controlled and a hydrophone line array was used to measure radiating noise in the towing tank. In addition, FEM was used to simulate underwater radiated noise induced by the impulse vibration of a submerged and watertight steel circular cylindrical shell. The effects of the cylindrical shell's structural configuration and the wall thickness on the sound radiation field were investigated. Previous experimental and FEM simulation studies in this area are reviewed below.

In (Wawrzynowicz *et al.*, 2014), the acoustic sound insulation performances of cement and foamed composite materials were studied via FEM simulation to analyze the transient and steady states of two-dimensional and three-dimensional models. In addition, experimental measurements were made to compare sound absorption rates. The results generated by the both models for both transient and steady states agreed with the experimental curve. In (Rawat *et al.*, 2015), the vibration response of a three-dimensional cylindrical liquid tank subjected to three-

dimensional transient seismic waves was studied by an acoustic-structural FEM. This was used to explore how the force induced by liquid shock water pressure coupled with the vertical force of the seismic wave to dynamically affect the tank bottom.

In (Junger, Feit, 1986), two thin-shelled cylindrical shells with different aspect ratios were subjected to an excitation force, and an analytical solution was obtained for the sound pressure level (SPL) in the far field. In (Wu, Too, 2021), underwater steady-state noise was generated and measured in a watertight steel circular cylindrical shell submerged in a towing tank, and the simulation results of the towing tank were consistent with the experimental results. This verified that FEM is feasible for the analysis of underwater sound radiation induced by continuous machine vibration in a towing tank. Thus, experimental measurements and FEM simulation can be used to analyze the radiated sound field generated by an underwater vehicle containing an operating machine. In an earlier study (Wu *et al.*, 2022), the characteristics of the boundary was an important factor to the accuracy of measurements and simulations for underwater radiation in a towing tank. The experiment was conducted to vibrate the watertight cylinder and to measure the underwater sound field, which was significantly impacted by reflections from the tank walls. The experimental measurements and underwater sound field simulations were consistent with each other at 45 and 250 Hz. The simulation and experiment were slightly larger in the 500 Hz case. The result was the simulations investigated the factors affecting the towing tank's boundary effects. In (Leader *et al.*, 2013), the sound and vibration of a torpedo-shaped structure under axial force excitation were experimentally investigated, and in (Wang *et al.*, 2000), machine vibration-induced underwater acoustic radiation was studied. The simulation theories in the present study and the FEM for fluid-structure interaction have also been applied in (Wu, 1989; Wu, Chen, 2017; Etter, 2018).

Several studies have conducted underwater structure-borne radiated noise experiments and acoustic-structural coupling simulations (Yoshikawa, 1993; Rugonyi, Bathe, 2001; Matthew, 2004; Tong *et al.*, 2007; Qian *et al.*, 2012; Zhang *et al.*, 2016). These studies have used the FEM or the boundary element method to analyze underwater noise and study the fluid-structure coupling vibration performance of a submerged double-cylindrical shell of a ship. The vibroacoustic response of a shaft-hull system was also numerically and experimentally investigated (Lin *et al.*, 2016).

In a boundary study (Sacks *et al.*, 1995), the perfectly matched layer approach (PML) was devised – in which the acoustic pressure on a peripheral boundary is set to 0 – to indicate that the acoustic pressure on a radiation boundary was completely absorbed. This means that an appropriate increase in the absorption coefficient of the main control equation enables the control equation of the absorption layer to be transformed. In (Alvarez-Aramberri *et al.*, 2014), a method for performing calculations for the automatically matched layer (AML) approach, an advanced version of the PML technology, was devised. PML calculation accuracy is affected by absorbing layer parameters, which are determined by researchers. In contrast, the AML approach does not require the manual definition of the absorption layer grid. Instead, the absorption layer parameters are automatically defined based on a model, such that they meet the infinite domain boundary.

2. Basic methodology

Theoretically, the wave equation can obtain the transient and steady-state solutions of acoustic-fluid coupling, and the Helmholtz equation is only suitable for solving steady-state solutions. In this study, the steel block dropped onto the steel cylindrical shell is the transient solution to solve the fluid-solid coupling. Therefore, the ABAQUS software uses the wave equation to derive the transient acoustic-fluid coupling solution first, and then derives the fluid-solid coupling solution.

The response of underwater noise generated from transient structural vibration can be directly derived from the wave equation. That is, the response is discretized from the sound domain, and thus the coupled transient acoustic-structural equation can be derived. The structure is regarded as an elastic body surrounded by fluid, such that structural vibration generates a fluid load at the fluid-solid interface and sound pressure generates an additional force on the structure. Therefore, the structural dynamic equation and the wave equation in the fluid domain must be calculated. The displacement and sound pressure on the fluid-structure interface are obtained via model discretization and from the wave and motion equations, as in (ABAQUS, 2014). Then, based on the assumption that the fluid is an ideal acoustic medium, the wave equation of sound pressure in a three-dimensional space is expressed as:

$$\nabla^2 P - \frac{1}{c^2}\frac{\partial^2 P}{\partial t^2} = 0, \tag{1}$$

where P is the instantaneous sound pressure, t is a time variable, and c is the velocity of sound in the medium, and

$$\nabla^2 = \left(\frac{\partial^2}{\partial x^2} + \frac{\partial^2}{\partial y^2} + \frac{\partial^2}{\partial z^2}\right). \tag{2}$$

The law of finite elements is used as an approximation method to calculate and obtain the solution of the wave equation. Equation (1) is thus rewritten as:

$$\nabla \cdot (\nabla P) - \frac{1}{c^2}\frac{\partial^2 P}{\partial t^2} = 0. \tag{3}$$

By applying the Galerkin approximation method, multiplying a sound pressure function of a boundary condition Φ, and integrating on the sound domain Ω, Eq. (4) is obtained:

$$\int_{\Omega} \Phi\left[\nabla\cdot(\nabla P)\right]\mathrm{d}\Omega - \int_{\Omega}\Phi\left[\frac{1}{c^2}\frac{\partial^2 P}{\partial t^2}\right]\mathrm{d}\Omega = 0. \tag{4}$$

From the chain rules of gradients:

$$u\left(\nabla\cdot\mathbf{v}\right) = \nabla\cdot\left(u\,\mathbf{v}\right) - \left(\nabla u\right)\cdot\mathbf{v}, \tag{5}$$

where $\mathbf{v}$ is the vector notation and u is a unit direction vector, therefore Eq. (4) can be written as:

$$\int_{\Omega}\nabla\cdot(\Phi\nabla P)\,\mathrm{d}\Omega - \int_{\Omega}\nabla\Phi\cdot\nabla P\,\mathrm{d}\Omega - \int_{\Omega}\Phi\left[\frac{1}{c^2}\frac{\partial^2 P}{\partial t^2}\right]\mathrm{d}\Omega = 0. \tag{6}$$

From the divergence theorem:

$$\int_{\Omega}\nabla\cdot\mathbf{A}\,\mathrm{d}\Omega = \int_{\Gamma}\mathbf{A}\cdot\mathbf{n}\,\mathrm{d}\Gamma, \tag{7}$$

where Γ is the boundary, $\mathbf{A}$ is an arbitrary vector, and $\mathbf{n}$ is the vector perpendicular to the boundary. In the fluid-structure interaction problem, Γ represents the water-structure contact surface; accordingly, Eq. (6) can be written as follows:

$$\int_{\Gamma}\Phi\nabla P\cdot\mathbf{n}\,\mathrm{d}\Gamma - \int_{\Omega}\nabla\Phi\cdot\nabla P\,\mathrm{d}\Omega - \int_{\Omega}\Phi\left[\frac{1}{c^2}\frac{\partial^2 P}{\partial t^2}\right]\mathrm{d}\Omega = 0. \tag{8}$$

By considering the water and the structure in the normal direction of the contact surface, the relationship between the water pressure gradient and structure is expressed as:

$$\mathbf{n}\cdot\nabla P = -\rho\,\mathbf{n}\left(\frac{\partial^2\mathbf{u}}{\partial t^2}\right), \tag{9}$$

where $\mathbf{u}$ is the displacement vector of the structure on the boundary surface. Equation (9) can also be written as:

$$\int_{\Gamma}\Phi\nabla P\cdot\mathbf{n}\,\mathrm{d}\Gamma = \int_{\Gamma}\Phi\left(-\rho\mathbf{n}\frac{\partial^2\mathbf{u}}{\partial t^2}\right)\mathrm{d}\Gamma. \tag{10}$$

Substituting Eq. (10) into Eq. (8) gives the following sound fluid equation:

$$\int_{\Omega}\Phi\left[\frac{1}{c^2}\frac{\partial^2 P}{\partial t^2}\right]\mathrm{d}\Omega + \int_{\Omega}\nabla\Phi\cdot\nabla P\,\mathrm{d}\Omega = -\int_{\Gamma}\Phi\rho\,\mathbf{n}\left(\frac{\partial^2\mathbf{u}}{\partial t^2}\right)\mathrm{d}\Gamma. \tag{11}$$

The known structural motion equation is:

$$\left[M_s\right]\left\{\ddot{U}\right\} + \left[C_s\right]\left\{\dot{U}\right\} + \left[K_s\right]\left\{U\right\} = \left\{F_s\right\}. \tag{12}$$

The sound fluid equation (Eq. (11)) is discretized and divided into several finite elements. Any point in the sound pressure elements and the displacement of the mass point are discretized with respect to time. This discretization can be performed through the interpolation of the corresponding value at the node of the element, and the sound pressure boundary condition function Φ can be eliminated. Equations (11) and (12) are thus combined into an acoustic-structural coupling equation as:

$$\begin{bmatrix}\left[M_s\right] & \left[0\right]\\ \rho\left[R\right]^T & \left[M_f\right]\end{bmatrix}\begin{bmatrix}\left\{\ddot{U}\right\}\\ \left\{\ddot{P}\right\}\end{bmatrix} + \begin{bmatrix}\left[C_s\right] & \left[0\right]\\ \left[0\right] & \left[C_f\right]\end{bmatrix}\begin{bmatrix}\left\{\dot{U}\right\}\\ \left\{\dot{P}\right\}\end{bmatrix} + \begin{bmatrix}\left[K_s\right] & \left[0\right]\\ \left[0\right] & \left[K_f\right]\end{bmatrix}\begin{bmatrix}\left\{U\right\}\\ \left\{P\right\}\end{bmatrix} = \begin{bmatrix}\left\{F_s\right\}\\ \left[0\right]\end{bmatrix}, \tag{13}$$

where $[M_s]$ is the mass matrix of the structure; $[M_f]$ is the mass matrix of the fluid; $[R]$ is the coupling factors; $[C_s]$ is the damping matrix of the structure; $[C_f]$ is the damping matrix of the fluid; $[K_s]$ is the stiffness matrix of the structure; $[K_f]$ is the stiffness matrix of the fluid; and $\{F_s\}$ is the structural load vectors.

The explicit dynamic-solver-analysis method is used with an extremely small time-step increment, as the setting of the time-step increment directly affects the simulation result in dynamic analysis. The central difference integration algorithm is used in the dynamic analysis to solve the overall balance equation for the entire operational process. Then, the dynamic equation is used to calculate the dynamic state of the next time-step increment. The dynamic balance equation for a single-degree-of-freedom system is expressed as:

$$m\ddot{u} + c\dot{u} + ku = p\left(t\right). \tag{14}$$

From the central difference theorem:

$$\dot{u}_i = \frac{u_{i+1} - u_{i-1}}{2\Delta t}, \tag{15}$$

$$\ddot{u}_i = \frac{u_{i+1} - 2u_i + u_{i-1}}{\left(\Delta t\right)^2}. \tag{16}$$

Substituting Eqs. (15) and (16) into Eq. (14) yields:

$$m\frac{u_{i+1} - 2u_i + u_{i-1}}{\left(\Delta t\right)^2} + c\frac{u_{i+1} - u_{i-1}}{2\Delta t} + ku_i = p_i. \tag{17}$$

Equation (17) can be rewritten as:

$$\left[\frac{m}{\left(\Delta t\right)^2} + \frac{c}{2\Delta t}\right]u_{i+1} = p_i - \left[\frac{m}{\left(\Delta t\right)^2} - \frac{c}{2\Delta t}\right]u_{i-1} - \left[k - \frac{2m}{\left(\Delta t\right)^2}\right]u_i. \tag{18}$$

According to Eq. (18), the displacement at a moment is related to that at the previous moment. The displacement, velocity, and acceleration of the model nodes are related to the incremental learning at each step. Therefore, ABAQUS/Explicit uses a very small initial time increment and many increment steps to complete the central difference method.

Equation (19) shows that in the time integration, the time increment directly affects the solution accuracy. The upper limit of the time increment is therefore used to obtain the stable value. In the absence of damping, the stable value of the time increment can be expressed as:

$$\Delta t_{\text{stable}} = \frac{2}{\omega_{\max}}. \tag{19}$$

However, several factors affect the frequency of a system, and sometimes its highest frequency cannot be accurately calculated. Therefore, another method is adopted to obtain a stable value, as shown in Eq. (20):

$$\Delta t_{\text{stable}} = \frac{L^{\varepsilon}}{C_d}, \tag{20}$$

where L^{ε} is the minimum length of the grid element, and C_d is the material wave velocity. Therefore, as the size of grid elements reduces, the time increment decreases accordingly, consistent with the time-stable incremental value.

In the FEM calculation, Eq. (13) is solved via the explicit integration method, and the derivatives of acceleration and velocity are replaced by central difference using the central difference method. Then, the state variable equation for the time before the small increment time is solved, and the effective load matrix and the effective load vector are calculated. This method can be used to calculate the dynamic instantaneous displacement condition of the next time increment within each tiny time increment, as in (ABAQUS, 2014).

In the ABAQUS software to perform transient micro-time step calculations, the software itself must have a high number of cores. This study only used a high-performance notebook computer CPU using 8 GB of RAM and one core calculations. Using the explicit dynamic solver, and setting the time period to 0.05 s, and each increment to 0.0001 s, the total calculation of 0.05 s took about 3 to 4 days. The operation time depends on the complexity of the structure and the length of the operation time. To speed up the computing speed, that can increase the computing cores of the software and increase the computing cores of the hardware.

3. Experimental measurement and analysis procedure

In this study, impulse excitation measurements were conducted to obtain the underwater radiation sound field. The architecture of the entire process was established via several experiments and simulation. The experimental measurement and analysis of the impulse-induced structural noise are described below. The procedure of the impulse-induced structural noise experiment is shown in Fig. 1.

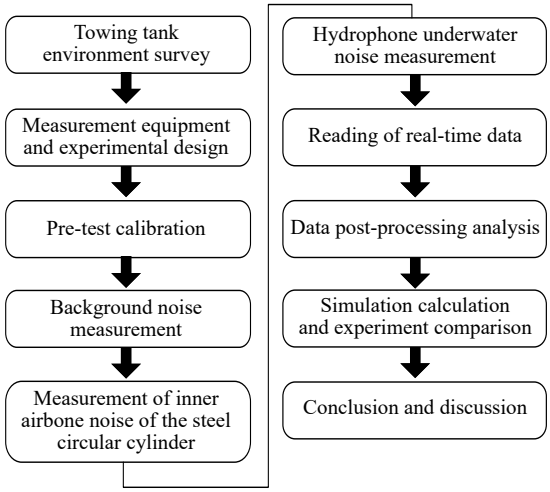

Fig. 1. Procedure of watertight steel circular cylindrical shell underwater measurement, and comparison with simulation results.

First, the towing tank was surveyed to confirm that it was sufficient to contain the watertight steel circular cylindrical shell. To ensure the feasibility of the experiment, the detailed experimental conditions were considered, such as the depth, environment, and background noise of the towing tank, and the capability of the tank to be hoisted on an experimental vehicle.

Second, the measuring vehicle was assembled and prepared. The 1 kg iron block was magnetically attached to the inside roof of the submerged watertight steel circular cylindrical shell and could be dropped by remote control to generate a vibration and noise that simulated an impulse-induced vibration noise radiated from an actual submerged vehicle (Fig. 2). The watertight steel circular cylindrical shell was designed (Fig. 3) so that it could be operated underwater and in air. The measuring instruments (a hydrophone, a sound level meter, and a microphone) were calibrated before measurement.

At the beginning of the underwater measurement, the background noise of the towing tank was measured. The sound level meter was used to measure the SPL of the airborne noise generated by the impulse excitation, and the underwater sound field of the hydrophone was measured. All measured values were converted via the fast Fourier transform (FFT) to obtain the frequency spectrum, and the values of repeated measurements were assessed to evaluate stability.

Many data were post-processed and analyzed to obtain the SPL of the underwater sound field. These data were compared with the FEM simulation data

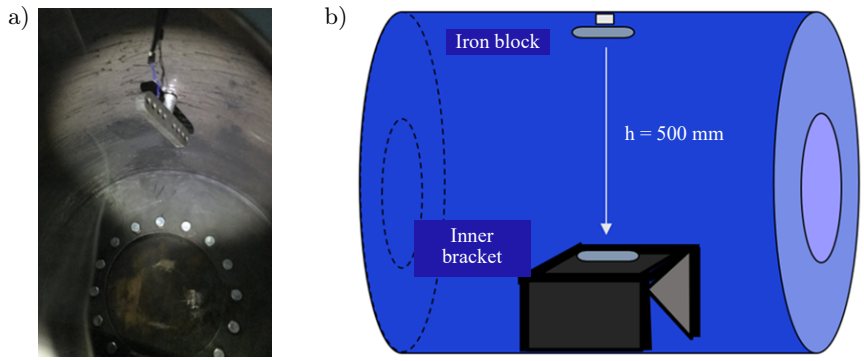

Fig. 2. Photograph of iron block magnetically attached to the roof inside a watertight steel circular cylindrical shell (a) and diagram of the full setup (b).

Fig. 3. Photograph of the watertight steel circular cylindrical shell being loaded into the towing tank (a) and the B&K 8104 hydrophone used to measure underwater noise (b).

for the water course direction of the towing tank. Finally, the characteristics of underwater sound radiation and the structural configuration of the vehicle were explored.

To obtain the radiation underwater sound field, the actual structural vibration of a fluid-structure interaction sound field was simulated using a numerical model and generated in an experimental model, with both models being of the same size and configuration. The underwater noise level was measured, and the results were compared with the FEM simulation results. The experimental measurement was conducted in the towing tank with a length of 176 m, width of 8 m, and depth of 4 m. The center of the watertight steel circular cylindrical shell was 1.5 m beneath the water surface.

The B&K 8104 hydrophone (Fig. 3b) with a measuring frequency of 0.1 Hz – 120 kHz was used for the underwater noise measurement. The frequency range and dynamic range of the microphone were 5–20 000 Hz and 182 dB re 20 μPa, respectively. The SPL and frequency ranges of the sound-level meter were 28–141 dB and 20 Hz – 8 kHz, respectively. In the experimental measurement, a four-by-one hydrophone line array was installed in the watercourse direction at 0.5, 1, 1.5, and 2 m in the towing tank (Fig. 4).

The hydrophones were connected to the signal extractor through an analog-digital converter. The data were collected at a sampling frequency of 100 kHz, the frequency spectrum was obtained via FFT, and data were transmitted to a computer for storage. In addi-

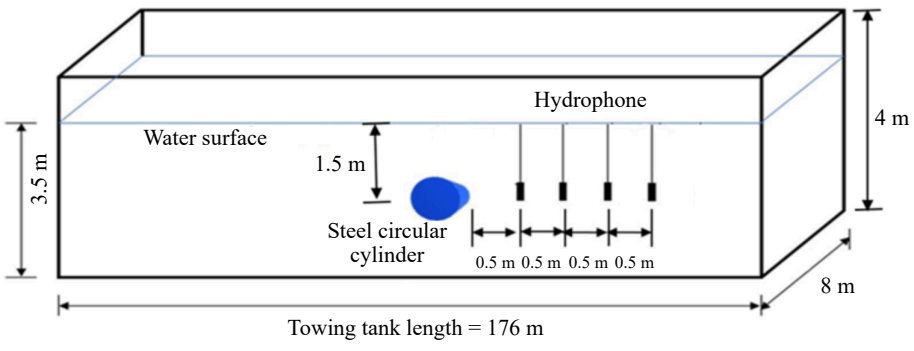

Fig. 4. Underwater configuration of hydrophone line array and the watertight steel circular cylindrical shell.

tion, the SPL of the inner airborne noise in the watertight steel circular cylindrical shell was measured using a sound level meter and was used to estimate the airborne source noise power induced by structural vibration. The iron block had an initial velocity V_0 of 0 mm/s and was positioned at a height of 500 mm above the bottom of the inner bracket surface of the watertight steel circular cylindrical shell. The velocity

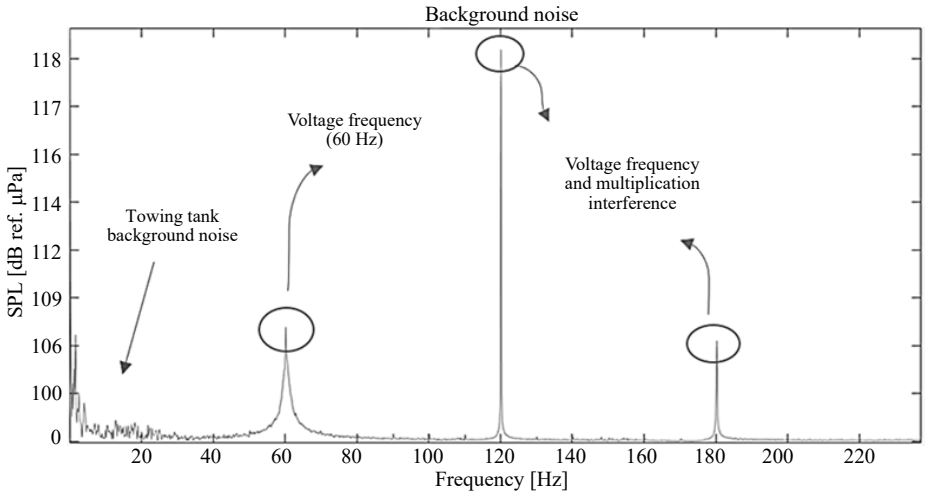

Fig. 5. Towing tank background noise measurement in the frequency domain.

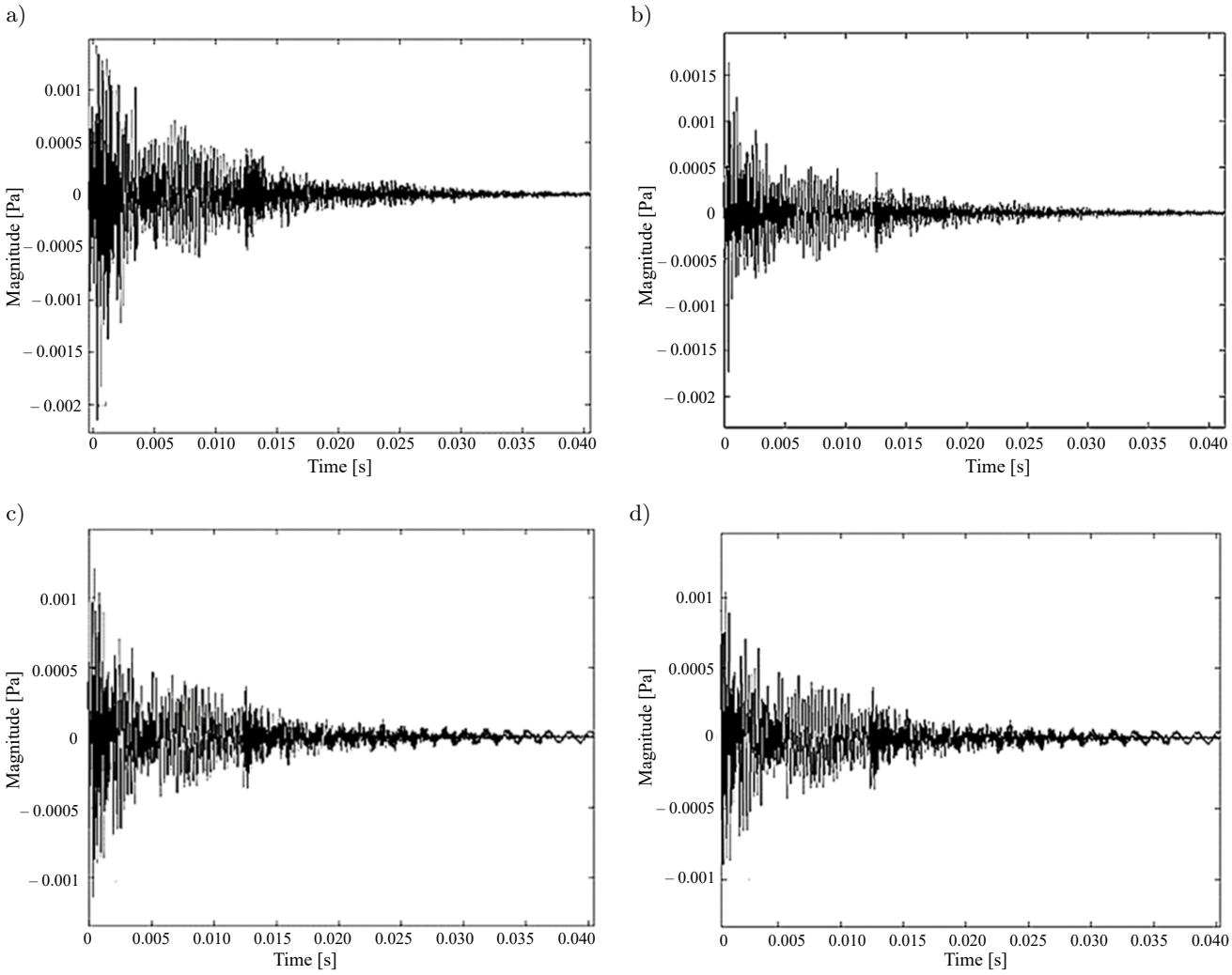

Fig. 6. Measured time series data of underwater acoustic pressure at 0.5 m (a), 1.0 m (b), 1.5 m (c), and 2.0 m (d) from the steel circular cylindrical shell.

of the iron block immediately before its impact with the bracket was calculated according to the conservation of energy from the roof to the impact point. The airborne noise power and the velocity of the block before impact were used as inputs of the FEM model.

The experimental results revealed that the airborne source noise contributed much less than the impulse-induced vibration generated by the impact of the iron block to the underwater radiated noise. Hence, the contribution of airborne noise was ignored and only the velocity of the iron block before its impact with the bracket (i.e., before the impulse excitation) was used as an input for the simulation. Previous studies (Wu, Too, 2021) have indicated that the background noise of this towing tank is low-frequency noise (<20 Hz) as shown in Fig. 5; as this is much lower in frequency than the impulse-induced vibration noise, the towing tank background noise was ignored in the simulation process.

The watertight steel circular cylindrical shell was designed with the following specifications: a ring thin shell of 8 mm, a two-sided thick shell of 12 mm, and an inner bracket of 8 mm. It was also fitted with watertight adapters and electromagnet device control lines. The steel circular cylindrical shell (Fig. 3a) has a weight of 284 kg, a diameter of 0.803 m, and a length of 1 m. The loading balance block and iron block were 212 and 1 kg, respectively. The steel circular cylindrical shell was suspended in the towing tank with remote controlled cables and a hydrophone array.

Figure 6 shows the time series data measured from the hydrophone line array in the watercourse direction at 0.5, 1.0, 1.5, and 2 m. This indicates the magnitude of the underwater impulse-induced vibration noise and decay within 0.4 s. The measured time series data were converted via FFT to obtain the frequency spectra at 0.5 and 1.0 m (Fig. 7). The transient vibration caused by impulse excitation produced a broadband frequency spectrum. This broadband frequency spectrum was the nature frequencies of steel circular cylinder cylindrical shell in the water and the 374 Hz was the larger amplitude frequency as shown in Fig. 8. Therefore, the

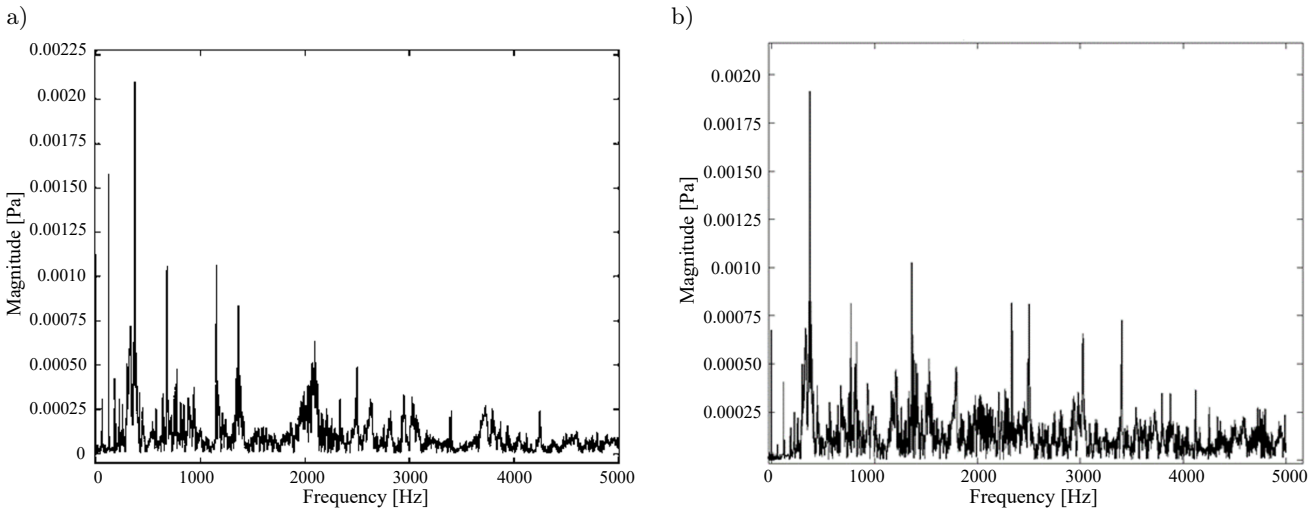

Fig. 7. Measured frequency spectrum of underwater acoustic pressure at 0.5 m (a) and 1.0 m (b) from the steel circular cylindrical shell.

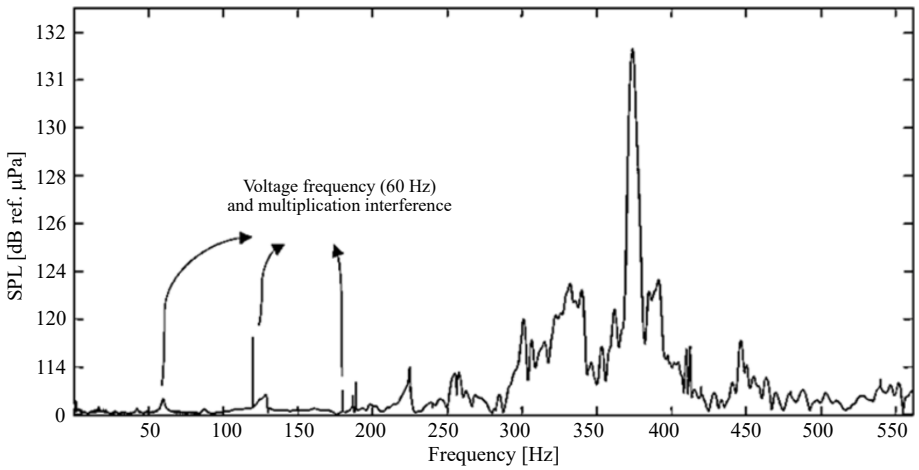

Fig. 8. Nature frequencies of steel circular cylinder cylindrical shell in the water and 374 Hz was the larger amplitude frequency.

peak magnitude of time series data was used for SPL calculation. The experimental results were compared with the FEM results, as presented in the next section.

4. Comparison of FEM simulation results with experimental results

The impulse-induced vibration noise radiated from the submerged steel circular cylindrical shell was also simulated via FEM, and the simulation results were compared with the experimental results.

The simulation results of the towing tank are in reasonable agreement with the experiment results, which demonstrates that FEM is a feasible method for analyzing underwater radiated noise. The simulation process is shown in Fig. 9.

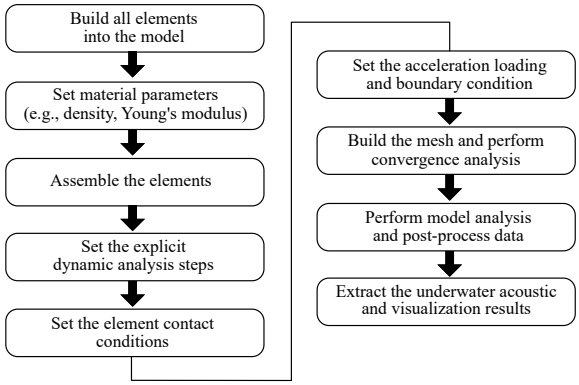

Fig. 9. Set the steps for the explicit dynamic analysis for the underwater vibration noise of impulse-excited structure.

A simulated model of the steel circular cylindrical shell was generated based on the experimental model and is presented in Figs. 10a and 10b, and Table 1, and the steel circular cylindrical shell payload was set to ensure that its weight and buoyancy in water were balanced, as shown in Table 2. The towing tank water model was established under loading and boundary conditions. The boundary condition of the water tank set the acoustic impedance at the bottom and both sides of the tank to approximately 4.3×10^6 kg/m^{2}s. The towing tank front and real walls were far away from the steel cylindrical shell and set non-reflection boundaries. The water surface boundary represents the pressure-release surface. The water surface was located above the steel circular cylinder, which was set in the center of the towing tank (Wu, Too, 2021). The towing tank model and boundaries were shown in Fig. 11 and the parameters were listed in Tables 3 and 4.

In the simulation, a dropped iron block modeled on the top of the bracket (Fig. 10b), as in the experiment. The impulse excitation caused a bracket vibration that was transmitted to the underwater radiated sound field. The parameters of the simulation of the iron block impulse excitation are listed in Table 5.

a)

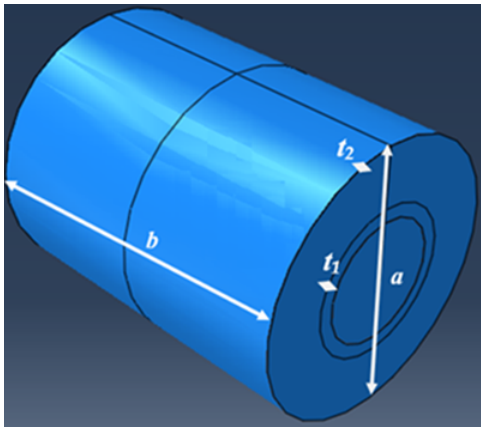

b)

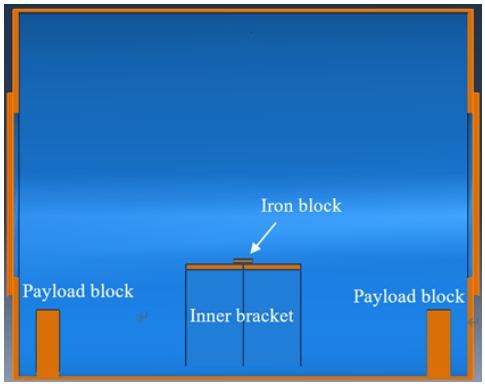

Fig. 10. Diagrams of the steel circular cylindrical shell model (a) and steel circular cylindrical shell inner configuration (b).

Table 1. Dimensions of steel circular cylindrical shell model.

Steel circular cylinder weight	284 kg
Thick round end-plate radius (a)	0.4015 m
Thick round end-plate thickness (t_1)	0.012 m
Thin shell cylindrical length (b)	1 m
Thin shell thickness (t_2)	0.008 m

Table 2. Dimensions of steel circular cylindrical shell payload model.

Payload weight	212 kg
Payload thickness (t_3)	0.01 m

Table 3. Properties of elements of the steel circular cylindrical shell materials in the model.

Elements	Steel circular, cylindrical shell, inner bracket, payload block and iron block
Material	Low-carbon steel
Young's coefficient (E) [GPa]	205
Poisson's ratio (υ)	0.3
Density (ρ) [kg/m^3]	7 850

Table 4. Dimensions of the towing tank model.

Towing tank dimension	$176 \times 8 \times 4$ m
Water density	1.0×10^9 tonne/mm^3
Water bulk modulus	0.139 MPa

a)

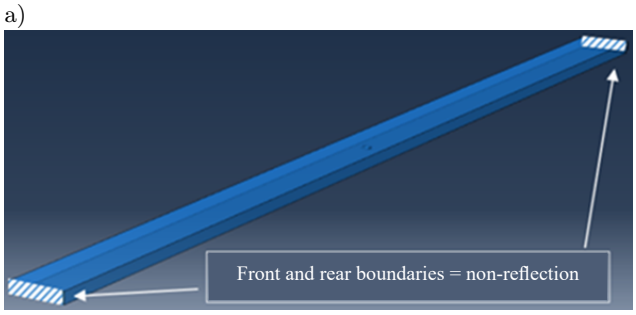

b)

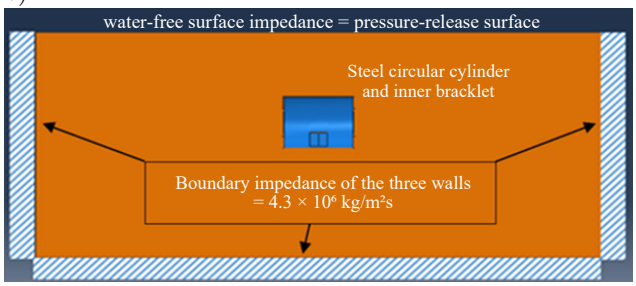

Fig. 11. Diagram of towing tank water model (a) and boundary conditions (b).

Table 5. Parameters of the simulation of the iron block impulse excitation.

Iron block weight	0.001 ton
Iron block dropping height (h)	500 mm
Gravitational acceleration (g)	9 800 mm/s^2
Initial speed (V_0)	0 mm/s
Final speed (V_1)	3 130.5 mm/s

Seed edges and gird types were set for the mesh grid geometry. Three-dimensional solid elements were used for analysis during the simulation. The mesh elements and grid quantities are shown in Table 6.

Table 6. Types of mesh and grid quantities for elements.

Element	Mesh grid type	Grid quantity
Towing tank	AC3D4	8 744 042
Steel circular cylindrical shell	C3D4	9 190
Inner bracket	C3D8R	1 872
Payload block	C3D4	1 477
Iron block	C3D8R	156

To confirm the correctness of the analysis results, the FEM was used for the convergence analysis. The grid quantity of a mesh directly affects simulation accuracy: a smaller mesh division yields more accurate analysis results than an larger mesh division. However, a mesh grid that is too small may generate too many nodes in a model, which may result in too many degrees of freedom and thereby make the model unstable and increase computational costs.

For the simulation of the sound pressure magnitude, the first hydrophone was placed at a certain distance from the steel circular cylindrical shell in the water tank. The comparison objects of grid quantity were analyzed. The grid dimension sizes and quantities are shown in Table 7.

Table 7. Mesh grid types and quantity.

Grid dimension Δx [mm]	Grid quantity
mesh125	14 289 405
mesh150	8 744 042
mesh175	5 681 363
mesh200	4 221 977
mesh225	3 561 442
mesh250	3 015 747

The grid analysis comparison was based on the sound pressure magnitude at 0.0008 s, and a convergence analysis of the water grid was performed. Grid dimensions Δx of 250 to 125 mm were used in the convergence analysis. The grid dimension was as shown in Fig. 12a. At a grid size of 150 mm and a quantity of 8 744 042, the sound pressure was 0.0017617 Pa. At a finer grid size (125 mm) and a higher quantity (14 289 405), the sound pressure magnitude did not change significantly (Fig. 12b). Therefore, a water tank grid size of 150 mm was chosen for further simulation analyses.

a)

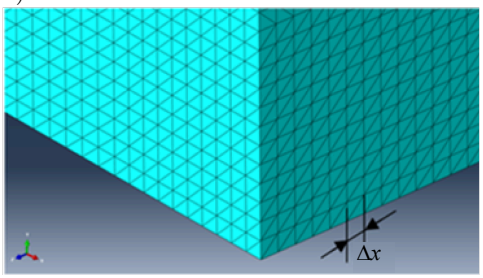

b)

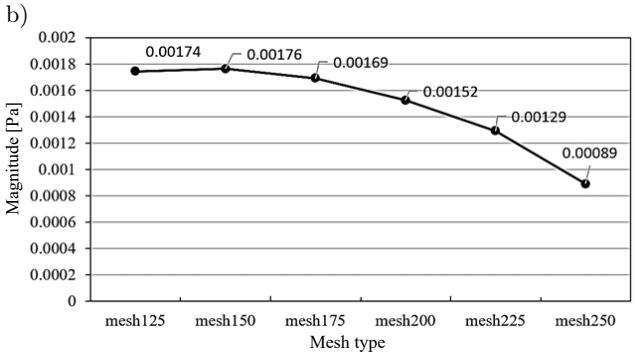

Fig. 12. Diagram of towing tank grid dimension Δx (a) and the convergence analysis of mesh types (b).

In the simulation study, four hydrophones revealed that the main energy occurred at 0–0.01 s. The energy gradually dissipated after 0.05 s and finally tended to be static and stable. The analog data from 0 to 0.001 s show that hydrophones at an interval of 0.5 m exhibited a difference in the vibration start time Δt.

The first hydrophone firstly starts to vibrate, and the second started to vibrate ~0.0003 s later, and this trend continued for the third and fourth hydrophones; Δt (0.0003 s) was exactly the time it took for the sound to travel 0.5 m in the water, as shown in Fig. 13.

The simulation analysis time was 0.05 s, and each increment was 0.0001 s. The underwater noise was transmitted through the bracket to the bottom of the steel circular cylindrical shell. The results show that the energy was concentrated within 0–0.01 s, and the energy gradually dissipated after 0.05 s (Fig. 14).

The transient vibration caused by impulse excitation produced a broadband frequency spectrum. Therefore, the peak magnitude of time series data was used for SPL calculation. The peak SPL results of the simulation were compared with the experimental results for each position of the underwater sound field. The peak magnitude of time series data was used for SPL calculation. The difference between the experimental and the simulated SPL was within 3 dB (Fig. 15 and Table 8), which demonstrated the high accuracy of the simulation.

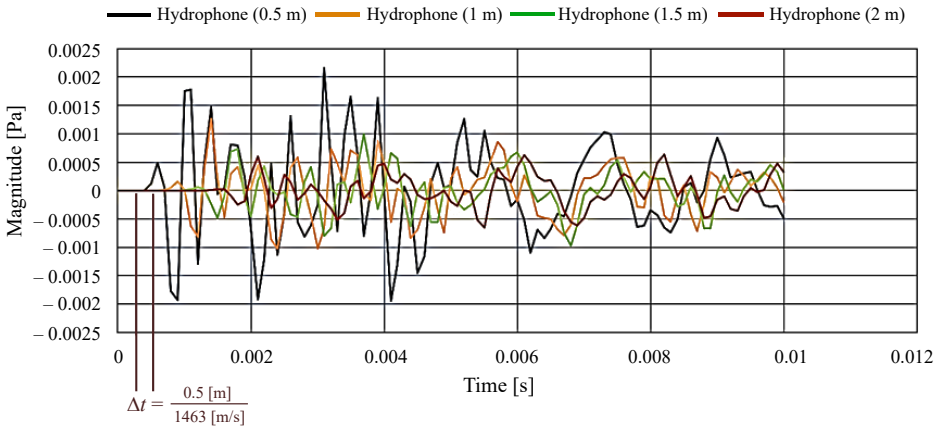

Fig. 13. Simulation of four hydrophones at 0.5, 1, 1.5, and 2 m with time delay Δt versus energy magnitude during $t = 0.01$ s.

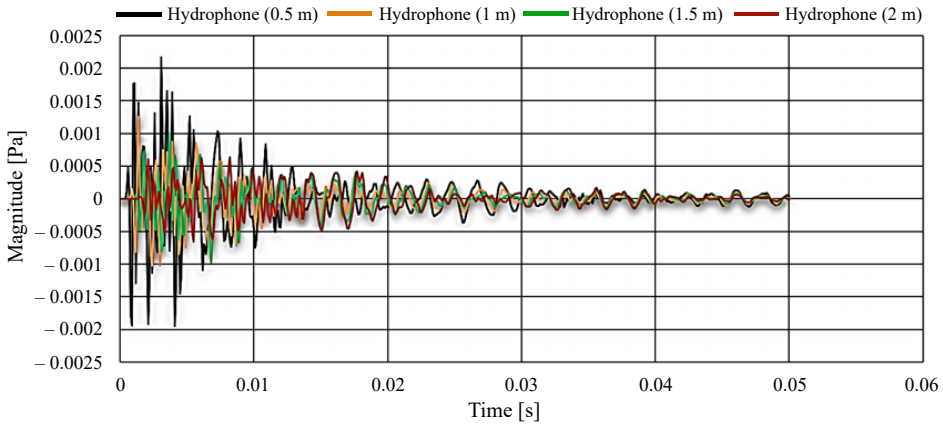

Fig. 14. Simulated underwater acoustic pressure time series data at 0.5, 1, 1.5, and 2 m from the steel circular cylindrical shell.

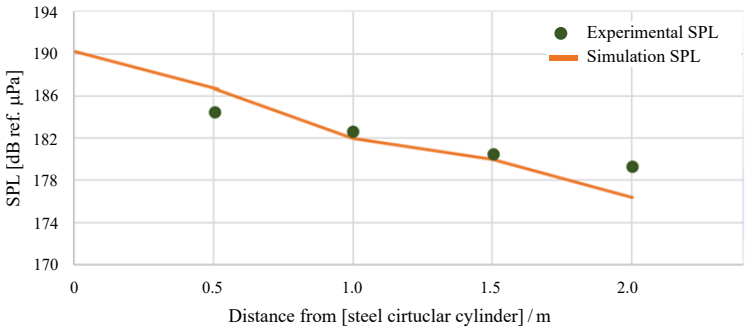

Fig. 15. Peak SPL in the towing tank watercourse direction.

Table 8. Comparisons of the simulated and experimental data of peak SPL in the towing tank watercourse direction.

Hydrophone location [m]	0.5	1.0	1.5	2.0
Experiment peak SPL [dB]	184.5	183.0	181.3	179.4
Simulation peak SPL [dB]	186.3	182.1	180.1	176.5
Discrepancy peak SPL [dB]	+1.8	−0.9	−1.2	−2.9

5. Influence of structural configuration on underwater sound radiation

In this section, the effects of structural configuration on sound propagation in the steel circular cylindrical shell and its radiation into water are discussed. The effects of the thickness, configuration, and shape of the steel cylindrical shell structure on the sound field are also discussed. The findings can be used as a design reference for the structural configuration of underwater vehicles. The effects are explored:

1) The dropping of the iron block to impact the base caused the structure below the circular cylindrical shell to vibrate and generate noise in water, which was followed by propagation of a sound wave in water (Figs. 16a–16c). A comparison of the thin shell with the thick end cap shows that the wave mostly came from the thin shell; that is, the main underwater sound was radiated into the water via the arc surface of the thin shell (Fig. 16).

2) After the impact of the iron block, the first acoustic sound wave radiated from the circular cylindrical shell bottom. The second sound wave was circularly diffused by the top arc surface of the thin shell of the cylindrical shell. The reinforced position of the bracket base structure acted as a truncation point for sound radiation in water (Figs. 17a–17c). The underwater sound was radiated from the perimeter of the unreinforced shell of the thin shell arc. This noise radiation behavior shows that the reinforcement position affected the propagation of structural vibration and could block the sound radiation integrity in water. The time series in Fig. 17 shows the sound radiation truncation, as indicated by the red arrows.

3) The underwater noise was radiated from the vibrating circular cylindrical shell to the bottom of the towing tank. The noise was diffused and reflected on both sides of the bottom (as indicated by the red circle in Figs. 18c and 18f).

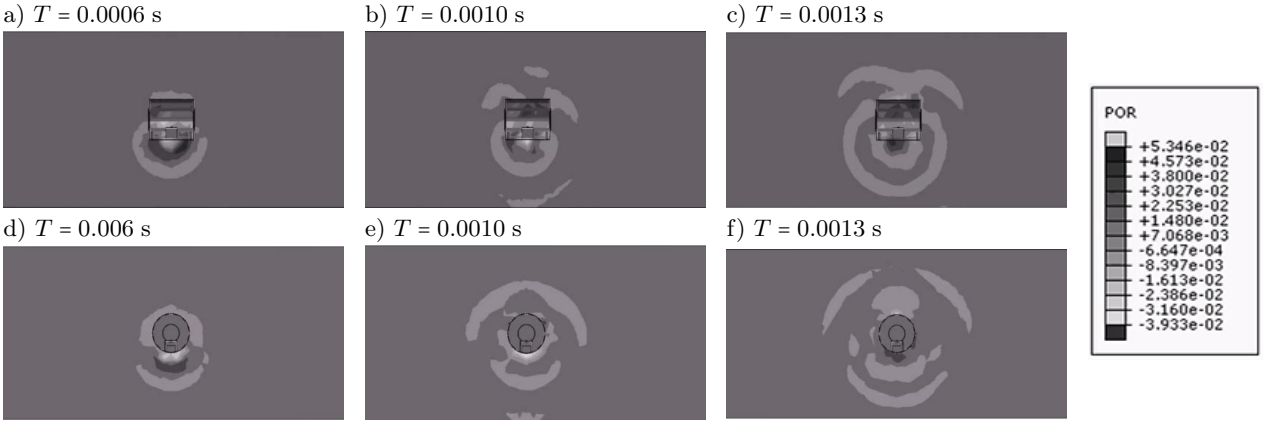

Fig. 16. Simulation diagrams of underwater noise transmitted from the arc surface of the thin shell to the water, where they form sound wave radiation.

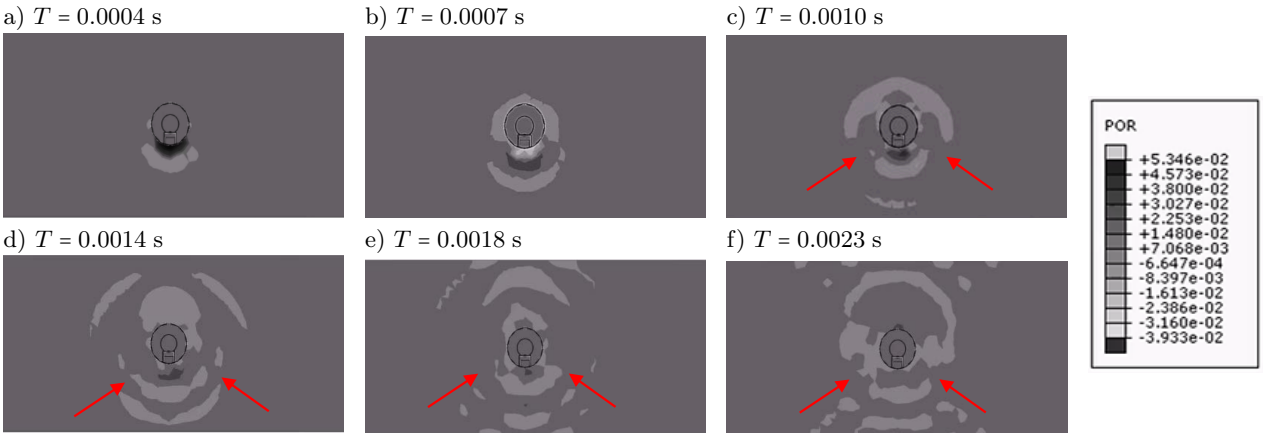

Fig. 17. Reinforced position of the bracket base structure and the truncation point of sound radiation in water.

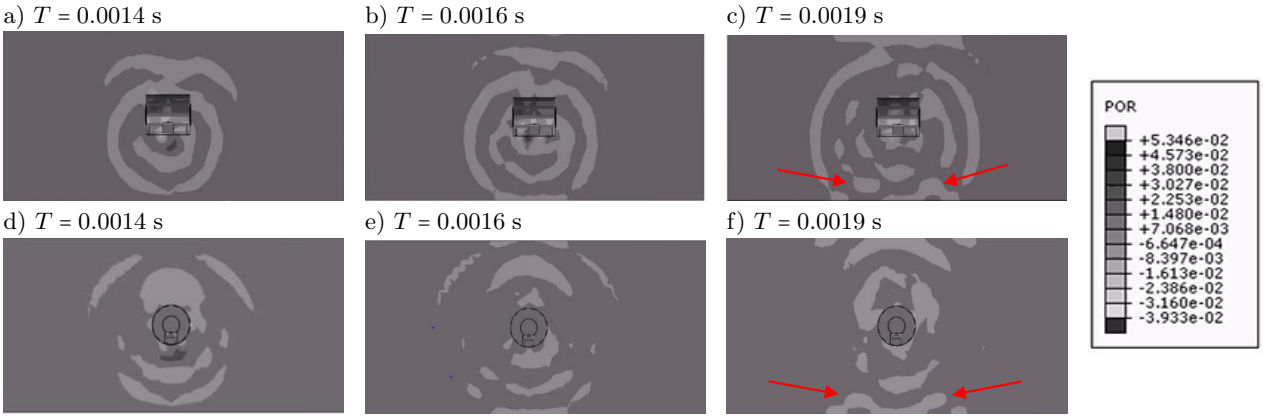

Fig. 18. Noise radiation patterns: noise diffusion and reflection on both sides of the bottom.

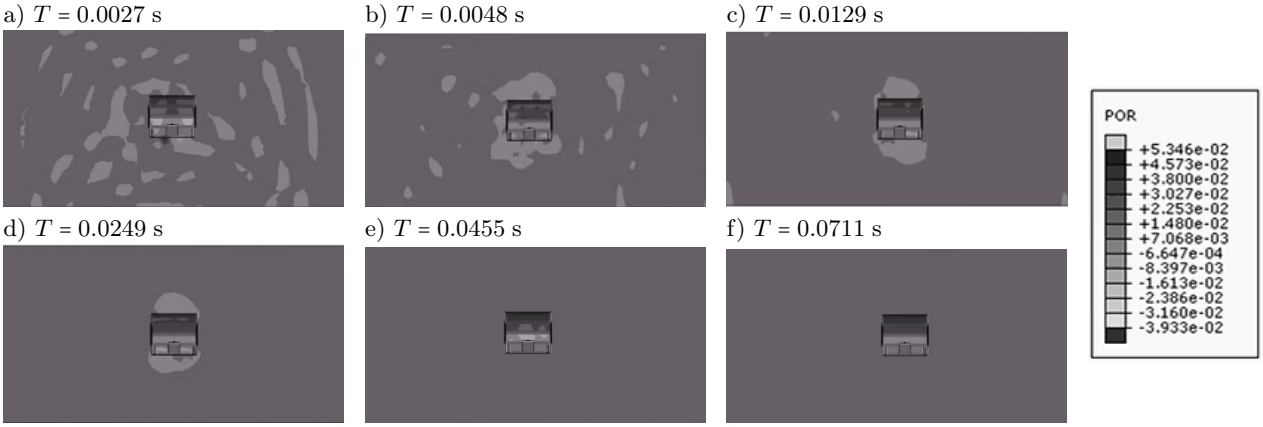

Fig. 19. Transmission of underwater noise from a structure with a gradually declining vibration energy.

4) When the vibration energy of the structure in the circular cylindrical shell was large, the vibration alternated from up to down and left to right. The acoustic sound was transmitted by the arc surface of the thin shell and the edges of both sides of the thick end caps (Figs. 17a–17c). With increasing reverberation time, the vibration energy gradually reduced and was transmitted only from the arc surface of the thin shell (Figs. 19c and 19d). Then, with decreasing vibration energy, the acoustic sound reverberated only in the circular cylindrical shell and ultimately disappeared (Figs. 19e and 19f).

6. Conclusions

In this study, impulse-induced structural vibration noise radiated by a watertight steel circular cylindrical shell in a towing tank was measured. Then, this experiment was simulated using the FEM. The accuracy of the simulation results was improved by adding an impulse speed to the loading conditions; as such, the simulation results were consistent with the experimental results. This demonstrates that it is a reliable simulation method for predicting the radiation of an underwater vehicle sound field caused by transient structural vibration. During the vehicle design process, the underwater noise and observed noise radiation can be predicted and analyzed via the finite-element method.

This study also explored the influence of structural configuration on sound propagation in a circular cylindrical shell and the radiation of this sound into the water. The thickness of the watertight steel cylindrical shell and the reinforced bracket base affected the underwater noise radiation. The thin shell of the structure was the main area from which sound was radiated, while the structural reinforcement position was the diffusion breakpoint of the underwater sound radiation. Therefore, a thicker and more complex reinforced structure will radiate less and incomplete sound into water.

According to the results of this study, although large underwater vehicles have complex structures, usually the main complex and large structures are installed at the bottom of the equipment. Therefore, regardless of the shock vibration of the equipment or the impact of the tool falling, the simpler structure of the upper part of the underwater vehicle is the easiest to radiate noise. The sound-absorbing material can

be covered in the appropriate position of the upper structure. Future research should be able to use the results of this study to conduct more in-depth research and investigate the noise characteristics, structural arrangement and sound-absorbing material performance of specific underwater vehicles.

Acknowledgments

This research was funded by the Ministry of Science and Technology of the Republic of China (project no. MOST111-2221-E-006-071).

References

1. ABAQUS (2014), *Abaqus Analysis User's Guide 6.14: Acoustic, Shock, and Coupled Acoustic-Structural Analysis*, Volume II, Part III, Chapter 6.9.1.
2. Alvarez-Aramberri J., Pardo D., Barucq H. (2014), Automatically adapted perfectly matched layers for problems with high contrast materials properties, [in:] *14th International Conference on Computational Science*, **29**: 970–979, doi: 10.1016/j.procs.2014.05.087.
3. Etter P.C. (2018), Noise I: Observations and physical models, [in:] *Underwater Acoustic Modeling and Simulation*, 5th ed., pp. 291–294, CRC Press.
4. Junger M.C., Feit D. (1986), Sound radiation by shells at low and middle frequencies, [in:] *Sound, Structures, and Their Interaction*, pp. 321–365, MIT Press, Cambridge.
5. Leader J., Pan J., Dylejko P., Matthews D. (2013), Experimental investigation into sound and vibration of a torpedo-shaped structure under axial force excitation, *The Journal of the Acoustical Society of America*, **133**(5): 3517, doi: 10.1121/1.4806301.
6. Lin C., Wang J., Qu Y., Zhang Z., Hua H. (2016), Numerical and experimental investigation on vibro-acoustic response of a shaft-hull system, *Engineering Analysis with Boundary Elements*, **71**: 129–139, doi: 10.1016/j.enganabound.2016.07.016.
7. Matthew H. (2004), The measurement and behavior of vibration, [in:] *Vehicle Refinement: Controlling Noise and Vibration in Road Vehicles*, Cranfield University, pp. 234–268, Elsevier, UK.
8. Qian D.-J., Miao X.-H., Wang X.-R. (2012), Sound radiation of underwater structure based on coupled acoustic-structural analysis with ABAQUS, *Applied Mechanics and Materials*, **226–228**: 2249–2252, doi: 10.4028/www.scientific.net/AMM.226-228.2249.
9. Rawat A., Matsagar V., Nagpal A.K. (2015), Finite element simulation of cylindrical liquid storage tank under tri-directional components of earthquake, *Journal of Structural Engineering*, **42**(1): 28–39, doi: 10.3850/978-981-09-1139-3_089.
10. Rugonyi S., Bathe K.J. (2001), On finite element analysis of fluid flows fully coupled with structural interactions, *Computer Modeling in Engineering and Sciences*, **2**(2): 195–212, doi: 10.3970/cmes.2001.002.195.
11. Sacks Z.S., Kingsland D.M., Lee R., Lee J.-F. (1995), A perfectly matched anisotropic absorber for use as an absorbing boundary condition, [in:] *IEEE transactions on Antennas and Propagation*, **43**(22): 1460–1463, doi: 10.1109/8.477075.
12. Tong Z., Zhang Y., Zhang Z., Hua H. (2007), Dynamic behavior and sound transmission analysis of a fluid-structure coupled system using the direct-BEM/FEM, *Journal of Sound and Vibration*, **299**(3): 645–655, doi: 10.1016/j.jsv.2006.06.063.
13. Wang W.-H., Liou J.-H., Sutton R., Dobson B. (2000), Machine vibration induced underwater acoustic radiation, *Journal of Marine Science and Technology*, **8**(1): 30–40, doi: 10.51400/2709-6998.2451.
14. Wawrzynowicz A., Krzaczek M., Tejchman J. (2014), Experiments and FE analyses on airborne sound properties of composite structural insulated panels, *Archives of Acoustics,* **39**(3): 351–364, doi: 10.2478/aoa-2014-0040.
15. Wu C.-I., Too G.-P. (2021), On underwater sound radiation in a towing tank induced by continuous machine vibration in a steel circular cylinder, *Journal of Mechanics*, **37**: 597–608, doi: 10.1093/jom/ufab026.
16. Wu C.-I., Too G.-P., Wu B.-H. (2022), The boundary acoustic impedance effects of a towing tank underwater sound radiation induced by a steel cylinder continuous vibration, *Applied Acoustics*, **201**: 109101, doi: 10.1016/j.apacoust.2022.109101.
17. Wu H.-T., Chen P.-T. (2017), Application of coupled FEM/BEM on the analysis of underwater radiated noise of a surface ship induced by hull vibrations, *Journal of Marine Science and Technology*, **25**(2): 196–204, doi: 10.6119/JMST-016-1118-2.
18. Wu X.-F. (1989), Faster calculations of sound radiation from vibrating cylinders using variational formulations, *Journal of Vibration, Acoustics, Stress, and Reliability in Design*, **111**(1): 101–107, doi: 10.1115/1.3269803.
19. Yoshikawa S. (1993), Fluid-structure coupling by the entrained fluid in submerged concentric double-shell vibration, *The Journal of the Acoustical Society of Japan (E)*, **14**(2): 99–111, doi: 10.1250/ast.14.99.
20. Zhang Y., Lou J., Yu X. (2016), Underwater vibration and acoustic radiation calculation of double cylindrical shell by three-dimensional sono-elasticity of ships, *Journal of Vibroengineering*, **7**: 18–24, https://www.extrica.com/article/17328.